Automated analysis of multiple performance characteristics in magnetic resonance imaging systems

Michelle M. Covell,[a] David O. Hearshen,[b] Paul L. Carson,[c] Thomas P. Chenevert, Paul Shreve, Alex M. Aisen, Fred L. Bookstein,[d] Brian W. Murphy, and William Martel

Department of Radiology, School of Medicine, The University of Michigan, Ann Arbor, Michigan 48109

(Received 26 August 1985; accepted for publication 30 July 1986)

As with other digital imaging systems in heavy medical use, it is desirable with magnetic resonance imaging (MRI) to obtain extensive, rigorous system performance measures from a small set of images of one or two relatively simple test objects. Digital analysis of the parallel square rod (PSR) test object introduces digital image system self-evaluation to MRI and extends automated image evaluation to include rigorous measures throughout the imaging volume rather than just average measures over the image. Precise comparisons with theory and between systems can be performed as well as quality control and corrections for nonuniformities. The PSR test object consists of an $18 \times 18 \times 36$ cm rectangular acrylic container enclosing 60 parallel square acrylic rods running the entire length. The inter-rod space is filled with a liquid or gel that produces strong, tissuelike signals in MRI and high contrast relative to the rods for computed tomography (CT). For profiles of slice thickness and separation, the rods are tilted in the test object to intersect the image plane at a 45° angle when the test object sides are parallel and perpendicular to the image plane. The test object itself is rotated 6–12° about its major axis so that the sides of the rods make a small angle to the rows and columns of pixels. This allows digital sampling at finer spacing than the pixels for determination of edge response functions. Over the 25–49 blocks in each slice of the imaged volume, maxima, minima, mean values, variances, and ratios currently are reported for the following variables: signal-to-noise ratio and sensitivity, linear and nonlinear image distortion, full width at half maximum (FWHM) resolution of the point spread function (PSF), slice separation, and slice thickness. These performance values at each rod or edge are displayed as gray scale functional images. Individual rod values are recorded and plotted as histograms and profiles. Results of the automated analysis for MRI system examples are in good agreement with expectations from theory and more manual tests.

INTRODUCTION

System performance of magnetic resonance (MR) scanners depends on many factors. The performance parameters can be classified into two groups: (1) those that depend upon the digital nature of the acquired signals and thus are similar to other imaging modalities such as computed tomography (CT), and (2) those which are dominated by magnetic resonance effects. Since MR images depend jointly upon these parameters in a complicated way, it is necessary to develop a set of standards and rigorous spatial measurements that will characterize image quality. These measurements should also allow for direct comparison of results from different MRI or CT scanners.

Quantification of MR images involves calculation of tissue specific characteristics: T_1, T_2, and density of the imaged nuclei. The signal intensities used to calculate these quantities depend upon the characteristics of the machine as well as the choice of a model for relaxation. It is important to separate machine dependence from inadequacies of the relaxation model when comparing relaxation times within the imaging volume and between machines. Prior investigations[1–8] have shown that variation in T_1 and T_2 measurements is influenced by inaccurate flip angles, motion and/or flow, and inadequacies of the models used to obtain the values. Several authors have shown that imperfect slice definition can lead to errors in T_1 of up to 100%.[2,3] Others have shown that errors of similar magnitude can occur when the rf field is nonuniform across the image plane or from slice to slice.[5,8] Diffusion during long echo delay times is also a source of error, which is dependent upon field gradients as well as echo time.[9] In addition to these effects, imperfect selective 180° pulses can lead to errors in intensity in multiple-echo techniques.[10,11] While analysis of the test object does not result in a direct measure of the accuracy of T_1 and T_2 calculated values, the analysis does provide information about parameters such as rf nonuniformity and slice definition which indirectly affect the accuracy of relaxation time calculations or any other quantitative measures.

Since the acrylic rods are much denser than the filling material, the parallel square rod (PSR) test object works well for CT as well as MRI, although the analysis program has not yet been run on CT images.

Automated analysis

Earlier system performance measurements in MRI have been accomplished with a variety of test objects using methods that were laborious and subjective.[1,12–14] Further complicating standardization of system parameters is lack of consistency in the definition of signal-to-noise ratio (SNR),[15–17] and normalization of signal when there are inaccuracies in slice thickness.[2,3] More importantly, in most approaches a complete set of quality control (QC) tests re-

 0094-2405/86/060815-09$01.20

quire multiple image acquisitions. This places requirements on machine time which severely limit the performance of routine QC tests.

We have developed an automated image analysis program for measurement of five performance parameters: image SNR, spatial distortion, spatial resolution, slice thickness, and slice separation. The program has edge-finding and edge-response capabilities for 90° edges (resolution) and 45° edges (slice thickness). The analysis programs are written in the language C,[18] and are running under UNIX on a VAX 11/780 computer in the Electrical Engineering and Computer Science Department at the University of Michigan.

MATERIALS AND METHODS

Test object description

The test object is a rectangular parallelopiped, $18 \times 18 \times 36$ cm, constructed of polymethyl methacrylate (acrylic). It contains rectangular rods oriented at 45° to the 18×18 cm faces of the container. The rods are glued to $\frac{1}{8}$-in.-thick acrylic plates to hold the rods in place. These rods are at 45° to two of the four 18×36 cm faces and parallel to the other two 18×36 cm faces (Fig. 1). Space between the rods is filled with a material that produces strong MRI signals and thus high contrast with the signal-free acrylic. The space between the rod configuration and the outside casing is filled with the same material, producing a signal that defines the outside boundary of the test pattern.

The test object is filled with 400-μM manganese chloride ($MnCl_2$) and phosphate buffered normal saline which has a T_1 of 325 ms as determined at 25 °C in the Diasonics MT/S imager using T_I = 1000 and 2000 ms at 15 MHz. A more rigorous measurement in a research spectrometer yielded a T_1 of 312 ms at 20 MHz. Per liter total volume, this test object solution consists of 8.48 g NaCl, 1.14 g sodium phosphate, dibasic (Na_2HPO_4), 0.28 g sodium phosphate, monobasic NaH_2PO_4, 0.079 g $MnCl_2(H_2O)_4$, 0.5 g sodium azide. The buffer provides physiologic *p*H and ionic strength, and the sodium azide is an algaecide.

Manganese-doped normal saline is employed as the dominant constituent of the phantom filler fluid to approximate patient electrical conductivity and dielectric coefficient more closely that manganese-doped pure water. Magnetic susceptibility is similar for all water-rich tissues, water, and saline. rf penetration, and therefore spatial uniformity of SNR and coil loading, should be closer to that of the average patient with saline than with pure water. Thus parameters such as measured SNR and the spatial variation therein should be relevant to the clinical situation, but the numbers are still affected somewhat by the size, configuration, and other electromagnetic properties of the phantom, which have not been matched rigorously to average patient heads and bodies. Coil tuning does appear to be well within the range encountered in clinical imaging, an observation which is not true for all MRI phantoms we and others have employed. Regarding eddy currents in the salinelike liquid, the presence of the acrylic rods tends to break up larger electrical current loops, as much, and probably more so, than do the most poorly conducting tissues in the body.

When properly positioned, the image of the small cross section of the test object has a checkered appearance (Fig. 2). We define a high-signal block (HSB) as the image of the signal from $MnCl_2$ bounded on all four sides by acrylic, and a low-signal block (LSB) as the image of the region occupied by an acrylic rod and base plates and bounded on all four sides by $MnCl_2$. The word "block" is used when the distinction between a HSB and a LSB is not necessary.

The test object is configured and positioned so that the two perpendicular sets of rod edges (Fig. 1) may be used in simultaneous measurements of slice thickness and separation for either vertical or horizontal resolution in the image. Those edges of the rods that are at 45° to the test object casing and, with proper positioning, to the image plane, will be

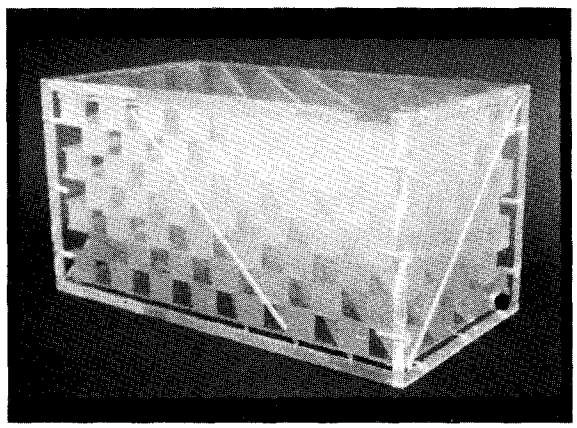

FIG. 1. Two faces of the test object. The small cross section approximates the transverse cross section of an average human head, and the large cross section approximates the cross section of an average human torso. Each 1-in. square rod was machined separately and attached to an acrylic plate. The seven rows of rods thus formed were assembled layer by layer. This results in the rows being separated by an extra 1/8 in.

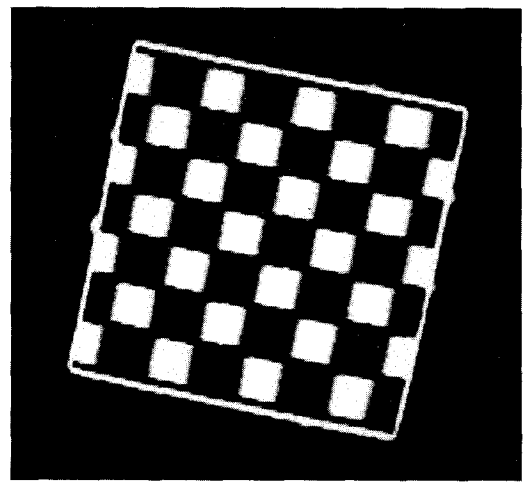

FIG. 2. Test pattern. The small cross section gives this MR image. The "90°" edges are at 102° with the vertical and the "45°" edges are at 12° with the vertical. The isolated signal pixels around the boundary of the pattern (one at the top and bottom and two on each side of the image) are from the diagonal grooves in the test object casing (see Fig. 1 and text). The position of these signals enables the user to locate precisely the physical position of the image within the object.

smeared over a distance proportional to the convolution of the slice thickness and the in-plane resolution. The signal from edges perpendicular to the casing and to the image plane will express the edge response function. By tilting the test object in the image plane so that this second set of rod edges is at a small angle to the horizontal, the sampling interval for computing profiles of signal intensity across the edges can be decreased.[19,20] In all the images shown (Figs. 2, 3, 5–10) the test object has been rotated 12° in the image plane, by means of an acrylic wedge support.

A larger angle is employed with this parallel rod phantom than in previous configurations[19] because of the need to sample completely across one or more pixel widths in the relatively small 2.54-cm dimensions of the blocks. At 12° the blurring is one-fifth of a pixel width for square pixels. The minimum angle for pixels 1.6 mm on a side is 6°; smaller angles could be employed with smaller pixels. A representation of the test object on its stand in the bore of the magnet is shown in Fig. 3. The acrylic produces low signal, represented by the dark blocks in the figure. The large cross section is shown on end, looking down the bore of the magnet.

On the outer faces of the test object we machined signal-generating diagonal grooves. The grooves on parallel faces of the test object are identical, except for one groove wider than all the rest. These grooves enable the user to determine the proper orientation of the phantom.[13] The widest groove uniquely labels one side of the image so that the absolute position of the test object within the imaging volume can be reproduced.

User interaction

MR images of the test object are processed to determine SNR, image distortion, and spatial resolution within and perpendicular to the image plane. The user specifies the image dimensions and the expected pixel size, and interactively determines the tilt angle of the test object within the plane. All further processing on a uniform image may be completed without user intervention.

Edge finding

The external edges of the test object are found by setting a threshold or "break point" halfway between the mean signal levels of two particular blocks. The first block has the maximum signal from the two central rows and columns of HSB's; the second has the minimum signal from the same two central rows' LSB's (see Fig. 2). The outside limits of the test object are set at the outermost pixel locations in contiguous rows and columns having values above the break point. Linear regression on this set of points is used to form a quadrilateral (Fig. 4). These best-fitting lines are used in all the subsequent analyses to describe the outside test object edges. Internal HSB's are located by finding contiguous areas of pixels above the same break point. If the area of a block is at least one-half the area expected in a HSB, it is treated as a valid block; otherwise, it is discarded. The edges of each block are then determined by the same method used to find the outside edges of the test object.

Edge response

Pixels across an edge are sorted by distance from the edge. The edge response of a rod edge lying perpendicular to the image plane is dependent only on the system's edge response function [Fig. 5(a)] while the edge response of a rod edge at 45° to the image plane is the convolution of the slice thickness profile and the edge response function [Fig. 5(b)]. When the slice thickness is several times larger than the image resolution, the user might choose to neglect the contribution of resolution as we have done to date and retain a good

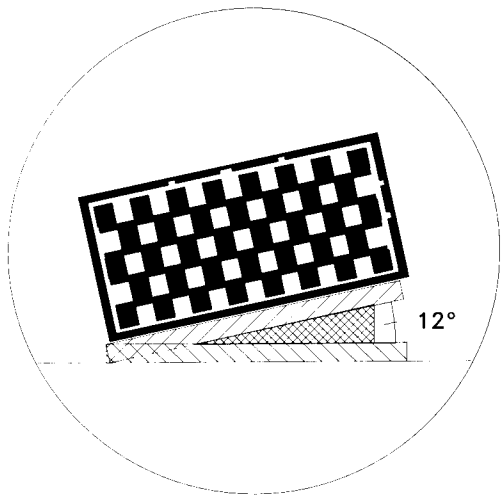

FIG. 3. Large cross-section representation of the test object. An axial plane is shown looking down the bore of the magnet. The wedge is positioned at 12° to provide better sampling of the edges of the blocks (see text). The intersection of the acrylic rods and the image plane is represented by the dark blocks.

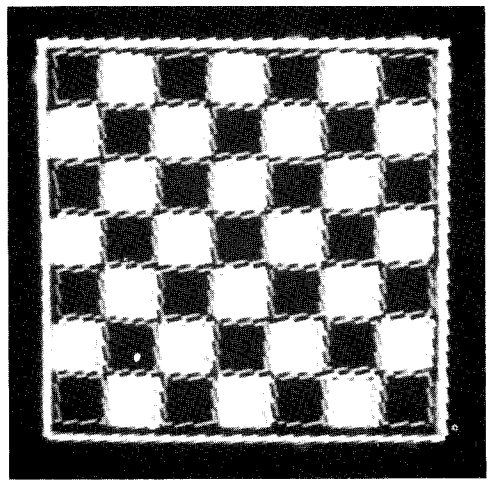

FIG. 4. Edge-fitting image. The edge of each signal and nonsignal block was computer fit, as described in the text. The computer-generated lines are shown as a gray border around nonsignal blocks and a bright border around signal blocks. The border is generated by a least-squares fit to the outermost set of pixels as described in the text (see Fig. 2).

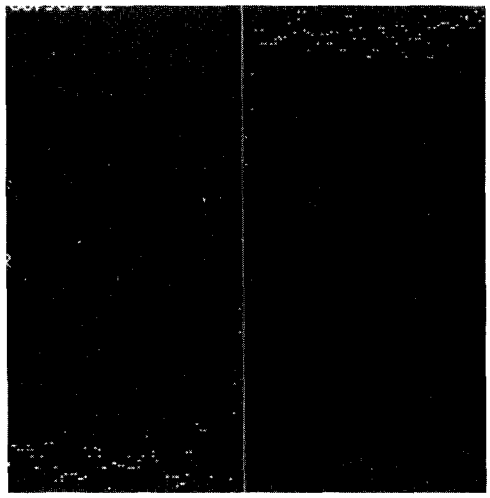

(a)

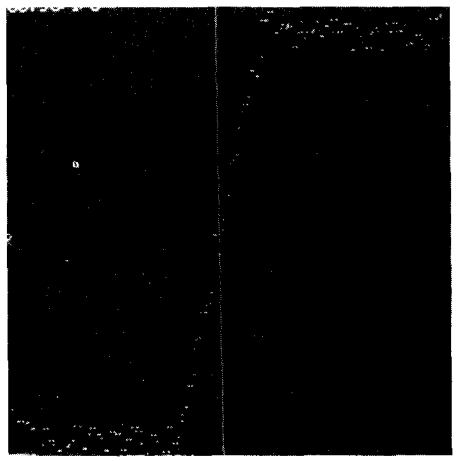

(b)

FIG. 5. Edge profiles for (a) resolution and (b) slice thickness. Each point in both images represents the gray level (intensity) of a pixel in or both of the two blocks that share a common edge. In both images shown here, the nonsignal blocks are on the left. Because the test object is rotated within the image plane, each pixel near the edge will be at a different distance, thus increasing the sampling of the edge. The curves generated represent (a) the edge response function and (b) the edge response function convolved with the slice profile. The middle section of the profile in (b) is actually at 45° to the vertical but appears to be at a lesser angle, due to scaling in the visual display.

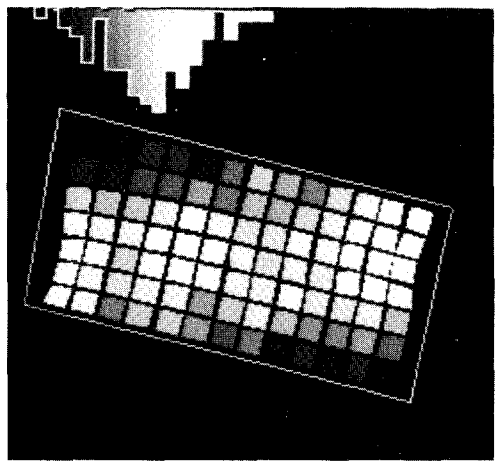

(a)

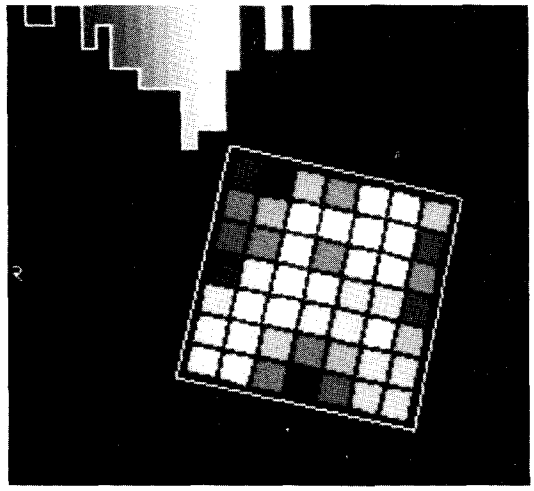

(b)

FIG. 6. SNR functional image for the large [Fig. 5(a)] and small [Fig. 5(b)] cross section of the phantom. The value of SNR, as defined in the text, is displayed for each HSB, and the values for the LSB's are interpolated from their nearest neighbor HSB's for display purposes. The values are then mapped onto the gray scale for display in two different formats: (1) the gray level of a block is directly proportional to calculated SNR for that block, and (2) these same values are used to construct the histograms displayed in the upper left-hand corner of each image. The histogram gives a visual display of the distribution of SNR's in the image. From left to right, lower gray levels in the histogram correspond to lower SNR's in the image. The spatial trend in SNR is primarily a result of rf nonuniformity across the field of view, and is thus a coarse mapping of the rf field.

measure of slice thickness for quality control purposes. The true slice thickness, however, can only be obtained by a deconvolution.

Image analysis output

Statistical analysis

Each block in the image plane is evaluated for each performance measurement. The values for each block as well as the mean, standard deviation, maximum, and minimum for the entire image are available on hard copy. The output is available in either the complete form, or a summary of the average measurements for the image.

Functional images

Measurements of scalar quantities are displayed as functional images: the value of each measurement is displayed in a gray scale at its location in the image field. A 20-section histogram of values is also provided in the functional image (Figs. 6–10).

The deformation tensor, which describes image distortion (see below), is displayed as a symmetric tensor field upon the distorted image. In two dimensions, the principal axes of the local deformation tensor are displayed as a cross with arms proportional to the strains in those directions (Fig. 7).

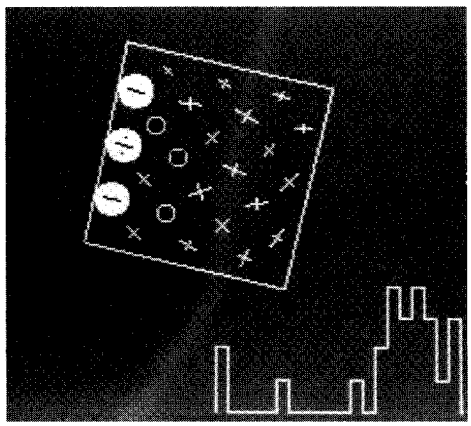

(a)

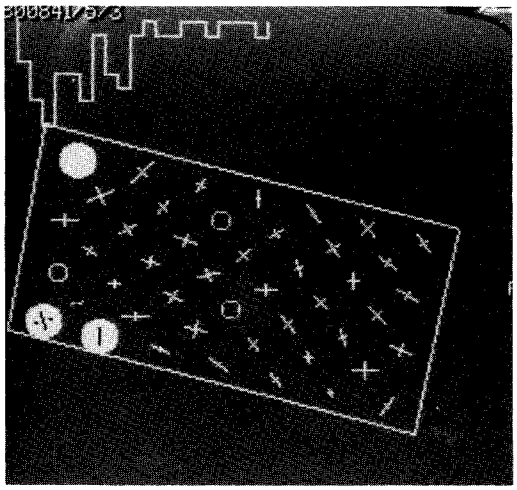

(b)

FIG. 7. Geometric distortion functional image of (a) the small cross section and (b) the large cross section of the test object. The principal axes of the local deformation tensor are displayed as defined in the text. The black tips of the crosses show tensor lengths less than the expected values, representing a "compression." The small circles represent deviations from the expected values of less than 2%, while the large circles represent deviations greater than 10%.

Signal-to-noise ratio

For each block, the mean and standard deviation of the pixel values are taken over all pixels inset from the block edges by a predetermined margin. The SNR in each block is defined as the ratio of the mean pixel value to the standard deviation of the pixel values in that block. The standard deviation includes noise from the material, image artifacts, large scale image inhomogeneity, and several other effects in addition to system electronic noise. The HSB and LSB pixel means, standard deviations, maxima, and minima are determined separately. The SNR's of the HSB's are displayed in a functional image (Fig. 6).

Image distortion

We define the distortion of each block as the deformation from an isosceles right triangle that has been constructed from the expected dimensions of the block, to a distorted triangle that is observed in the image of the block.[21] Specifically, the distorted triangle is constructed with its base taken as a diagonal of the imaged block. One corner of the block is rotated 180° about the diagonal and the average position of the two nearby corners is taken as the triangle's vertex. The deformation is treated as homogeneous over the triangle. With this definition, the deformation tensor can be calculated and formally related to the stress–strain tensor.[21] The principal strains are computed by a simple algebraic procedure.[22]

The transformation from the isosceles right triangle to the averaged distorted one will change a circle into an ellipse. The anisotropy is the ratio of the major and minor axes of that ellipse and is the ratio of the principal strains, i.e., the greatest relative change in any shape measure upon the block. This ratio thus gives some indication of the magnitude of the local distortion at each location. This measurement provides information used in the display of the deformation tensor. The tensor is displayed as a cross if the anisotropy is greater than 2%. Crosses corresponding to anisotropy less than 2% are not displayed, as their orientations are highly noisy. Instead, small open circles are displayed at these locations in the functional image (Fig. 7). In order to prevent compression of the scale, principal axis lengths deviating from unity by more than 10% are indicated by a filled-in circle: no attempt is made to display their true relative lengths. The deformation data for these blocks can be checked in the reported statistics.

A transformation between identical images would result in strains equal to unity (and no directional assignments). To emphasize the difference between the observed principal axis lengths and the normative expectation, deviation of the axis lengths from unity is indicated visually as follows: lengths below unity have the remaining length to unity blackened in; lengths above unity have the length beyond added on in white.

Local anisotropy values are displayed in a separate functional image (Fig. 8), and the means, standard deviations, and extrema are computed and printed out.

Resolution

The edge response profile across an edge between a HSB and a LSB and perpendicular to the image plane is fit piecewise to three lines: one in the region of the LSB, one in the region of the HSB, and one in the edge itself. For both resolution and slice thickness, straight lines rather than constants are fit to what would normally be the uniform low- and high-signal regions because of usually slowly varying image nonuniformities. These lines are fit to regions well outside the boundary and extrapolated to their intersections with the straight line which was fit to the boundary. A linear fit is employed for the boundary because the edge response profile is quite linear [Fig. 5(a)] as expected for the nearly rectangular point spread function reported by the manufacturer of our MRI system. The edge line is fit to the data between 10% and 90% of the expected pixel size, centered at the edge. The block lines are fit to the data beyond one pixel size from the edge.

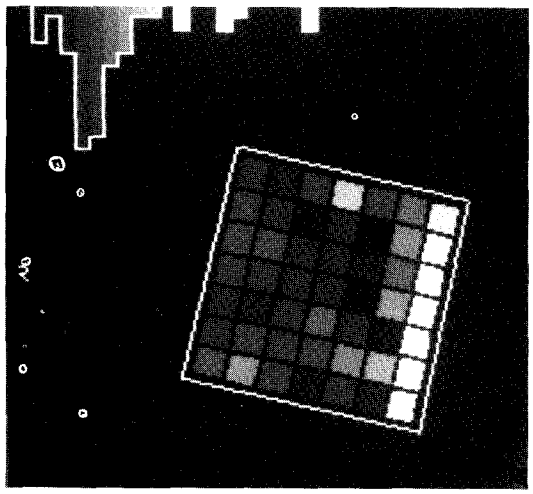

FIG. 8. Anisotropy image. The ratio of the two principal axes in Fig. 6(a) is displayed as a functional image. The gray level of each block is directly proportional to the calculated anisotropy of the block. The right side of the image corresponds to a high degree of distortion analogous to the visual interpretation of Fig. 6(a). The histogram gives a visual display of the distribution of anisotropy in the image. From left to right, lower gray levels in the histogram correspond to smaller anisotropy in the image.

The resolution at the edge is defined as 80% of the distance between the intersections of the edge line and the block lines. Clearly, resolution reported according to this definition will be 80% of the pixel size if the edge response function is a straight line, as would be the case if the point response function is rectangular and the resolution is pixel limited. The full width at half maximum (FWHM) of a Gaussian point response function will be quoted correctly by this method. The mean, standard deviation, maximum, and minimum of resolution are reported and the resolution on the various blocks is displayed as a functional image (Fig. 9).

Slice thickness

The edge response profiles across an edge rotated 45° to the image plane are analyzed for slice thickness in an analogous manner to the determination of resolution. The edge line is fit to the data between the 10% and 90% thresholds of the expected slice thickness, centered at the edge. A linear fit is performed in the HSB and LSB, one slice thickness from the edge. The slice thickness at the block is taken as the 10%-to-90% distance between the intersections of the edge line and the block lines. The mean, standard deviation, maximum, and minimum of slice thickness are computed and the slice thickness displayed in a functional image (Fig. 10).

The 10%–90% linear fit model employed will provide only a slight underestimate of the FWHM of the slice thickness if the derivative of the slice profile is Gaussian since the boundary is fit with a straight line rather than the true edge response of a Gaussian—the error function. As the derivative of the true slice profile approaches a rectangle, the 10%-to-90% distance provides a slice thickness measurement which is 1.25 times smaller than the width of the rectangle if the effects of pixel size are negligible or have been deconvolved. Ideally, such deconvolution should be performed and the appropriate model applied with necessary corrections. Even then, no single resolution or slice thickness number will provide a complete comparison between radically different profiles. The 10%–90% distance is merely a convenient measure which is close to the FWHM. Similar arguments are true for in-plane resolution.

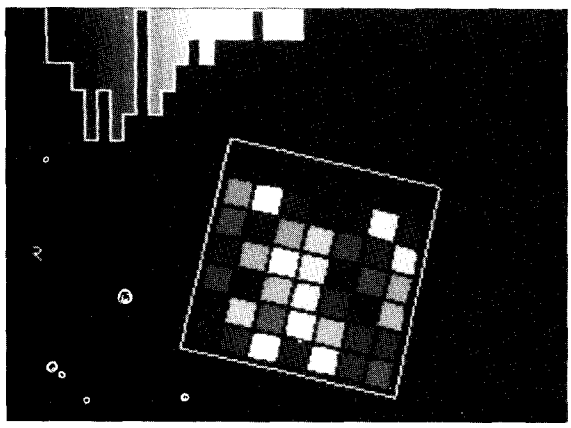

FIG. 9. Resolution image. Edge profiles are used to generate resolution values for display as a functional image. The gray level of each block is directly proportional to the calculated resolution for the block. Because two adjacent blocks are required to generate one profile, there is no value generated for the top row of blocks, i.e., the resolution value from an edge profile is coded onto the block below the edge. The histogram gives a visual display of the distribution of resolution in the image. From left to right, lower gray levels in the histogram correspond to higher resolution (smaller pixels) in the image.

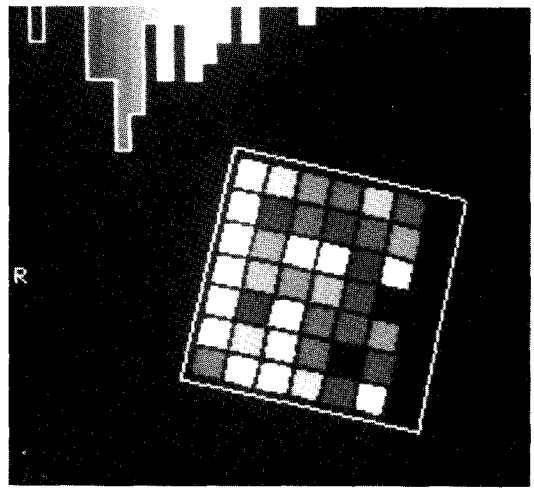

FIG. 10. Slice thickness image. In an analogous fashion to resolution (see Fig. 8 and text), profiles of 45° edges are used to calculate slice thickness. The gray level of each block is directly proportional to the calculated slice thickness at the block. For the orientation of the test object in this run, the 45° edges are vertical and generate profiles from column to column. The right-most column has no slice profile, i.e., the slice thickness values are mapped onto the block to the left of the edge. The histogram gives a visual display of the distribution of slice thickness in the image. From left to right, lower gray levels in the histogram correspond to smaller slice thickness in the image.

Slice separation

The separation between slices at a block is determined by comparing the relative locations of the block in the two slices. Since the edges are rotated at 45° to the slice plane, the offset between the two imaged locations will be the slice separation distance. The block locations are taken as offsets from the test object's outside edge, an edge perpendicular to the slices, avoiding errors due to side slipping of the image slices relative to one another. The mean, standard deviation, maximum, and minimum of slice separation are computed and the separation distances are displayed in a functional image (Fig. 11).

RESULTS

A point of concern has been whether convection currents in relatively nonviscous filling fluids, such as water with paramagnetic salts, would create motion artifacts. To test whether significant convection currents are created during imaging, two experiments were performed in the phantom enclosure without the rod structure insert. In one, dental floss of varying lengths was suspended throughout the saline from the top of the phantom. In the second, the phantom was half-filled with a solution of saline and red dye. Clear water was poured carefully over the saline to form a boundary with low surface tension between these two miscible fluids. No liquid motion was observed in either phantom arrangement during a 20-slice, spin-echo sequence with two echoes, and $T_R = 2.0$ s. This, and most other two-echo, multislice sequences, provide among the highest local maximum specific absorption rates available on our 0.35-T scanner (approximately 0.5 W/kG for a typical body). Therefore rf-induced fluid motion in the phantom is evidently not a problem for most 0.35-T systems with common pulse sequences. With the honeycomb of acrylic rod inserts in the parallel rod phantom, such fluid motion is probably insignificant for any MR system which remains below the FDA guidelines of 2 W/kG averaged over any gram of tissue.

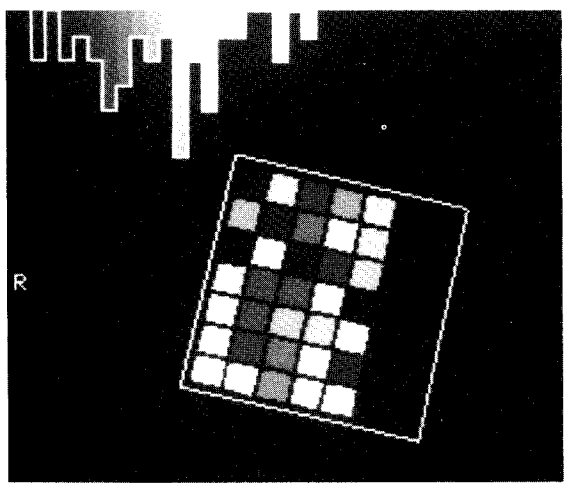

FIG. 11. Slice separation image. The displacement of a block between adjacent images, measured via distances between 45° edges and a fixed vertical edge of the border, is used to generate slice separation values for each block. The gray level of each block is directly proportional to the calculated slice separation at the block. The image is stored with the higher numbered slice (see Table I). For the same reason as slice thickness, the right-hand column of blocks is blank. The histogram gives a visual display of the distribution of slice separation in the image. From left to right, lower gray levels in the histogram correspond to smaller slice separation in the image. The distribution of the slice separation values for the small cross section is narrow, with no apparent spatial trends.

Analysis on two four-slice sets of images was completed. Both cross sections of the PSR test object were scanned using a body-sized rf coil. Both cross sections had $T_R = 2$ s, $T_E = 28$ ms, nominal pixel-limited resolution 1.7 mm, and nominal slice thickness 7 mm. The small cross section had a matrix size of 128×128 and a field of view 20 cm. The large cross section had a matrix size of 256×256 and a 40-cm field of view. The number of slices acquired in each case was 20 and the central four slices were analyzed. The results for the small cross section are summarized in Table I, and those for the large cross section in Table II. The mean and standard deviation, s, are given for each performance measurement.

While the evaluation measurements centered around the expected values, spatial trends were observable in SNR and distortion. Results of resolution and slice thickness measurements scattered more randomly. Spatial trends were most apparent in the analyses of the large (18×36 cm) cross sections. In both sets of images, comparable trends were found in neighboring slices, and, to some extent, in different runs with the same configurations.

DISCUSSION

Spatial distortions including the important one of anisotropy are easily quantified and characterized to a precision greater than that of clinical significance. In the University of Michigan (UM) MRI system, as in all whole-body scanners with which we are familiar, spatial distortion in the periphery of large fields of view is at a level which could be clinically significant. Precise anatomical correlations with CT, ultrasound, stereotactic techniques, biopsy guidance, and radiation therapy treatment planning are examples where spatial distortion should be characterized if not corrected. These measurements should be important in monitoring the movement of large masses of metal in the fringe field of the magnet and of small masses which may collect within the system.

The spatial variation in signal level and SNR is significant for visual image interpretations and also for quantitative tissue characterization by relative intensities or relaxation times. Although these spatial variations in signal level are inevitable consequences of coil design, monitoring of their spatial variation should be a sensitive measure of common problems, such as conductive or magnetic material within the bore, capacitative coupling within the coil housing, or between the rf coil and anything else, and eddy currents.

On the UM system, we do not see a marked spatial pattern in vertical or horizontal resolution, slice thickness, or separation. For example, there is no significant tilting of image planes relative to each other. However, such spatial variations are possible and their measurement is of concern to several manufacturers. Properties that can be easily measured with the test object manually or included in future

TABLE I. Summary of performance evaluation measurements; 18×36 cm cross section.

Measurement	Slice 30		Slice 31[a]		Slice 32		Slice 33	
	Mean	s	Mean	s	Mean	s	Mean	s
HSB[b]	762.1	45.0	752.1	42.5	752.3	36.0	749.5	39.0
LSB[c]	47.0	2.5	44.7	4.2	47.2	2.7	49.3	3.7
Anisotropy[d]	1.02	0.009	1.03	0.018	1.02	0.011	1.02	0.010
Resolution[e]	1.62	0.20	1.62	0.18	1.60	0.20	1.63	0.27
Slice[e] thickness	5.71	0.36	5.78	0.32	5.73	0.26	5.72	0.32
Slice[e] separation			10.07	0.18	10.16	0.21	10.28	0.24

[a] Slice 31 is the center slice of 20.
[b] High signal block SNR (ratio of the mean signal to the standard deviation of pixel values in a block).
[c] Low signal block SNR.
[d] Ratio of principal axes (see text).
[e] In millimeters.

automation include lateral displacement of images relative to others in the same sequence, Gibbs phenomenon and other ringing artifacts, spatial variation of noise in the LSB's or standard deviation in the HSB's (these are computed but not displayed separately at present), and centering and orientation of the various system components relative to each other.

Because this program uses a small amount of image display software and hardware that is system dependent available in the Electrical Engineering and Computer Science Department, it is not easily transportable to other systems. In addition, the edge detection algorithm may be inadequate when there are large distortions or low SNR in portions of the image. These two problems are currently being addressed and a more portable version is expected shortly.

CONCLUSIONS

Once quality control and higher performance evaluation techniques of sophistication are developed, they rarely are utilized routinely in medical imaging with the possible exceptions of scintillation imaging and film processing. In most radiologic imaging, technologists and service personnel do not perform and interpret adequate tests. Neither they nor the physicists usually have time for laborious complete performance tests or less complete routine tests and when these are performed there is neither standardization nor objectivity in the interpretation. Quality control of film processing is one example where there is an immediate return for the department, and this has been strongly supported by film suppliers.

Automated performance evaluation of images with the maximum number of relevant tests per image sequence would solve most of these problems. With improvements in computer technology it will soon be practical to perform complete analyses of test images routinely, and to automatically flag deviations from the norm. The test object and software presented here are directed toward that goal. With the described digital analysis of the edges and statistical analysis of multiple performance characteristics on a single test pattern, it is possible for a single-image sequence to replace the multiplicity of image acquisitions with various test sections or inserts as required in most CT and MR phantoms. Certainly test images should be acquired in a variety of conditions, such as coronal or oblique planes to verify proper system functioning, but the variety of tests would be much larger with most other phantom configurations, and not all tests would need to be performed at the maximum frequency.

Measurements also are made at many points throughout

TABLE II. Summary of performance evaluation measurements; 18×36 cm cross section.

Measurement	Slice 20		Slice 21[a]		Slice 22		Slice 23	
	Mean	s	Mean	s	Mean	s	Mean	s
HSB[b]	303.4	76.1	294.2	66.8	290.9	61.5	296.2	69.0
LSB[c]	18.0	2.3	21.3	3.2	16.1	1.4	18.5	2.3
Anisotropy[d]	1.07	0.048	1.06	0.044	1.06	0.031	1.07	0.060
Resolution[e]	1.61	0.20	1.59	0.19	1.60	0.17	1.61	0.19
Slice[e] thickness	6.35	0.45	6.21	0.37	6.28	0.36	6.23	0.38
Slice[e] separation			10.12	1.62	9.53	3.22	9.85	3.62

[a] Slice 21 is the center slice of 20.
[b] High signal block SNR (ratio of the mean signal to the standard deviation of pixels in a block).
[c] Low signal block SNR.
[d] Ratio of principal axes (see text).
[e] In millimeters.

the imaging volume. While the utility of this feature is obvious for establishing the useful field of view for coils, via signal levels or SNR's, and for in-plane image distortion, it is also useful for more complex distortion such as image plane tilting and thickness variation. Other than statistical precision, the value of multiple resolution measurements is yet to be established. Another important feature of this general approach is that it provides a more objective, reproducible measurement than does visual analysis. Only one test pattern is available in the phantom for most measures, thus increasing the likelihood that readily comparable measurements will become available on numerous and various scanners.

Perhaps the main value of the test methods, in addition to providing the otherwise laborious measurements of spatial distortion and spatial variation in signal or relaxation times, is that they provide an objective, reproducible measurement of resolution, slice thickness, and separation, at each location and averaged for each plane and with adequate statistics for high precision.

ACKNOWLEDGMENTS

Helpful information and feedback were provided by Dr. Howard Guenther, Dr. Joel Blank, and Ron Schilling of the Diasonics Corporation. Initial phantom tests and data acquisition were performed at the Huntington Medical Research Institute with the kind assistance of Dr. William Bradley. Dr. Charles Meyer provided guidance and many helpful ideas. Mr. Quentin Westrick very skillfully constructed the first few models of the PSR test object. This work was supported in part by the Diasonics Corporation and Grant No. PDT 242 from the National Cancer Society.

[a] Present address: Department of Electrical Engineering, Massachusetts Institute of Technology, Cambridge, MA.

[b] Present address: Department of Radiology, Henry Ford Hospital, Detroit, MI.

[c] Address correspondence to Paul L. Carson, Ph.D., University of Michigan Medical Center, 1500 E. Medical Center Drive, Radiology Department, Box 0030, Room XS2315, Ann Arbor, MI 48109, tel. (313) 763-5884.

[d] Present address: Center for Human Growth and Development, The University of Michigan, Ann Arbor, MI.

[1] L. Brateman, L. W. Jennings, and R. L. Nunnally, in Scientific Program, Society of Magnetic Resonance in Medicine, Third Annual Meeting, New York, 1984, pp. 98–99.

[2] D. J. Bryant, J. A. Payne, D. R. Bailes, and I. R. Young in Scientific Program, Society of Magnetic Resonance in Medicine, Third Annual Meeting, New York, 1984, pp. 109–110.

[3] I. L. Pykett, B. R. Rosen, F. S. Bunonamo, and T. J. Brady, Phys. Med. Biol. **6**, 723 (1983).

[4] R. L. Ehman, R. O. Kjos, R. C. Brasch, M. Brant-Zawadzki, and C. B. Higgins, in Scientific Program, Society of Magnetic Resonance in Medicine, Third Annual Meeting, New York, 1984, pp. 206–207.

[5] G. B. Matson, J. Magn. Reson. **56**, 200 (1984).

[6] W. T. Sobol, I. G. Cameron, J. C. MacTavish, L. J. Schreiner, and M. M. Pintor, in Scientific Program, Society of Magnetic Resonance in Medicine, Third Annual Meeting, New York, 1984, pp. 695–696.

[7] A. M. Aisen, G. M. Glazer, P. L. Carson, and D. O. Hearshen, Magn. Reson. Imag. **4**, 207 (1986).

[8] J. Granot, J. Magn. Reson. **53**, 386 (1983).

[9] E. O. Stejskal and J. E. Tanner, J. Chem. Phys. **42**, 288 (1964).

[10] J. Duijn, J. Creyghton, and J. Smidt, in Scientific Program, Society of Magnetic Resonance in Medicine, Third Annual Meeting, New York, 1984, pp. 197–198.

[11] E. L. Hahn, Phys. Rev. **80**, 580 (1950).

[12] E. L. Madsen and G. D. Fullerton, Magn. Reson. Imag. **1**, 135 (1982).

[13] V. M. Runge, G. Johnson, F. W. Smith, J. J. Erickson, R. R. Price, C. L. Partain, and A. E. James, Noninv. Med. Imag. **1**, 49 (1984).

[14] T. W. Redpath, Phys. Med. Biol. **27**, 1057 (1982).

[15] W. A. Edelstein, P. A. Bottomley, and L. M. Pfeifer, Med. Phys. **11**, 180 (1983).

[16] L. E. Crooks, M. Arakawa, J. Hoenninger, B. McCarten, J. Watts, and L. Kaufmann, Radiology **152**, 127 (1984).

[17] H. R. Hart, P. A. Bottomley, W. A. Edelstein, S. G. Karr, W. M. Leuer, O. Mueller, R. W. Reddington, J. S. Schenck, L. S. Smith, and D. Vatis, Am. J. Roentgenol. **141**, 1195 (1983).

[18] B. W. Kernighan and D. M. Ritchie, *The C Programming Language* (Prentice–Hall, Englewood Cliffs, 1978).

[19] P. F. Judy, Med. Phys. **3**, 233 (1976).

[20] S. M. Bentzen, Med. Phys. **10**, 579 (1983).

[21] F. L. Bookstein, J. Theor. Biol. **107**, 475 (1984).

[22] F. L. Bookstein, *The Measurement of Biological Shape and Shape Change* (Springer, New York, 1978).